Optics Communications 527 (2023) 128920

Contents lists available at ScienceDirect

Optics Communications

journal homepage: www.elsevier.com/locate/optcom

A Fabry–Pérot interferometer strain sensor composed of a rounded rectangular air cavity with a thin wall for high sensitivity and interference contrast

Qiao Li [a], Jianxin Wang [a], Haiwei Mu [a], Jingwei Lv [a], Lin Yang [a], Ying Shi [b], Zao Yi [c], Paul K. Chu [d], Qiang Liu [a], Chao Liu [a,*]

[a] School of Physics and Electronic Engineering, Northeast Petroleum University, Daqing 163318, China
[b] Institute of Unconventional Oil and Gas, Northeast Petroleum University, Daqing 163318, China
[c] Joint Laboratory for Extreme Conditions Matter Properties, Southwest University of Science and Technology, Mianyang 621010, China
[d] Department of Physics, Department of Materials Science and Engineering, and Department of Biomedical Engineering, City University of Hong Kong, Tat Chee Avenue, Kowloon, Hong Kong, China

ARTICLE INFO

Keywords:
Fabry–Pérot interferometer
Air cavity
Optical fiber sensor
Strain sensitivity
Interference contrast

ABSTRACT

A Fabry–Pérot interferometer (FPI) strain sensor with high sensitivity and interference contrast is designed and fabricated by a simple, cost effective, and safe process which can be scaled up for commercial production. The excellent strain sensitivity of 8 pm/με and interference contrast of 25 dB stem from the special structure with the unique air cavity, small wall thickness, and excellent reflection surface of the air cavity. The strain-temperature cross-sensitivity of the sensor is only 0.59 με/°C in the temperature range of 20–80°C. The sensor has large potential in applications such as strain sensing.

1. Introduction

Optical fiber sensors which have many merits such as compactness, fast response, and strong anti-electromagnetic interference are used in monitoring of electrical properties [1,2], refractive index [3,4], temperature [5,6], and strain [7,8] in many fields including health monitoring and biomedical engineering. There are two kinds of strain sensors. The first type is based on fiber gratings such as fiber Bragg fratings (FBGs) [9,10] and long period gratings (LPGs) [11] and the second kind is based on interference sensors such as Mach–Zehnder interferometers (MZIs) [12,13] and Fabry–Pérot interferometers (FPIs) [14–21]. Compared to other sensors, the air cavities in the optical fibers of FPIs [22] have smaller thermal expansion coefficients rendering them relatively insensitive to the environmental temperature leading to lower temperature-strain cross-sensitivity and more reliable strain measurement.

So far, various methods have been proposed to fabricate FPIs with high strain sensitivity by means of electrode discharge fusion splicing technique. For example, Li et al. have prepared a circular air cavity by fusing the single-mode fiber (SMF) and hollow-core photonic crystal fiber (HC-PCF) [14]. The strain sensitivity of the sensor is 3.36 pm/$\mu\varepsilon$ and the interference contrast is 4 dB. Duan et al. have preprocessed optical fiber tips to obtain two SMFs with cleaved flat tips and fusion induced hemispherical tips and then fused them to form an air cavity [15]. The strain sensitivity of the sensor increases to 4 pm/$\mu\varepsilon$ and the interference contrast is 7 dB. Cai et al. have proposed an asymmetrical air-cavity Fabry–Pérot interferometer (UAFPI) [21]. The air cavity is formed by welding and chemical etching of the erbium-doped fiber (EDF) and discharging multiple times on one side to form the taper. Compared to the conventional air-cavity Fabry–Pérot interferometer (AFPI), this sensor exhibits a high sensitivity of 10.15 pm/$\mu\varepsilon$ and interference contrast of 5 dB. However, these sensors require expensive PCFs and special optical fibers and the fabrication involves complex pretreatment and dangerous chemicals. For electrode discharge fusion splicing technique, manufacturing process parameters such as discharge time, discharge power and applied tensile stress have great influences on the cavity structures of the sensors, thus leading to different sensing performances. For example, the discharge time determines the radial expansion of air cavity and the flatness of the reflection surface on the air cavity wall. Therefore, further investigations are needed to improve strain sensitivity and interference contrast.

In this work, a simple and economical fabrication method is designed to prepare the Fabry–Pérot interferometer (RRAFPI) with a rounded rectangular air cavity. Two SMFs are fused to form the tiny air cavity and then different stresses are applied and discharged to produce the RRAFPI. The sensor has not only the unique characteristics of AFPI, but also a good reflection surface on the air cavity which improves the interference contrast. The selected parameters in this work can make the reflection surface of the cavity wall flatter and smoother, and bring

* Corresponding author.
E-mail address: msm-liu@126.com (C. Liu).

https://doi.org/10.1016/j.optcom.2022.128920
Received 14 May 2022; Received in revised form 22 August 2022; Accepted 25 August 2022
Available online 29 August 2022

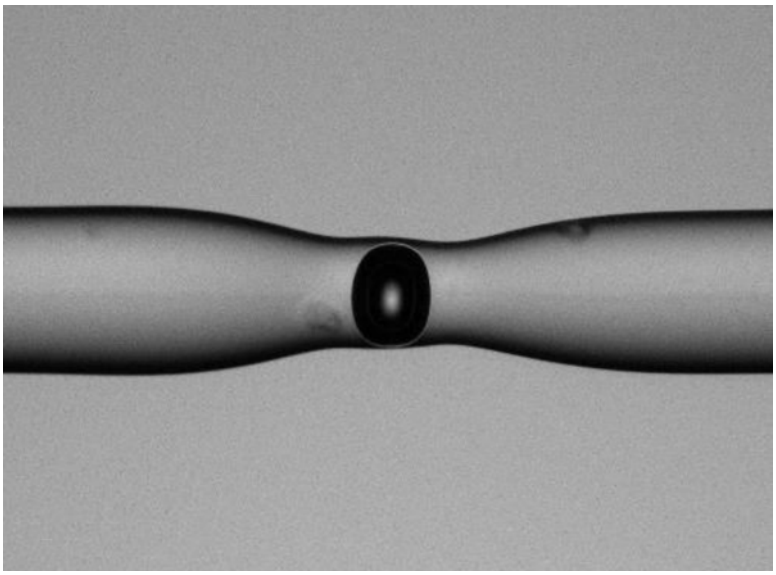

Fig. 1. Microscopic picture of the RRAFPI.

the angle of incident light closer to 90°, which in turn allows the sensor to have an interference contrast of up to 25 dB. The sensor has a strain sensitivity of 8 pm/$\mu\varepsilon$ at 1550 nm. In the temperature range of 20–80 °C, the temperature sensitivity of the sensor is 4.79 pm/°C and the strain-temperature cross-sensitivity [23–25] is only 0.59 $\mu\varepsilon$/°C. The interference contrast of the sensor is 25 dB that is almost four times that of AFPI.

2. Sensor fabrication and working principles

The microscopic image of the sensor is depicted in Fig. 1. The discharge power determines the bubble expansion speed and the final cavity wall thickness. A precise controlled discharge power thus reduces the wall thickness to achieve the goal of increasing the radius of the air cavity. But the wall thickness is too thin to reduce the strain measurement range. The wall thickness is about 1.3 μm. The rounded rectangular air cavity has a good reflection surface. The magnitude of the applied tensile stress determines the magnitude of the cavity length. Our precise control over tensile stress can result in a sensor cavity length of only 59 μm. This not only allows the strain sensitivity of the sensor to be further boosted, but also the small size of the cavity length has potential applications in micro strain monitoring and integration.

Fig. 2 shows the fabrication process of the sensor which is safe, simple, economical, and highly efficient. The coating of the SMF [26,27] was stripped and wiped clean with alcohol, The SMF was then cut into a flat tip by a fiber cleaver. To prepare the sensor, the fiber was placed in a fiber fusion splicer (Fujikura 80s) as shown in Fig. 2(a) and moved to the suitable position manually. The appropriate discharging power and discharging time were adopted to obtain the hemispherical tip as shown in Fig. 2(b). Anther SMF was processed by the same way and the tips of the two SMFs were dipped into a small amount of refractive index matching liquid (Nd: 1.47), so that the two SMFs formed a liquid film on the tips before placing in the optical fiber fusion splicer as shown in Fig. 2(c). Fig. 2(d) illustrates the application of extrusion stress. In the process, the two SMFs were moved by a motor to contact each other but leaving a small displacement to apply the stress. The discharging power and time of the fusion splicer were adjusted so that the two SMFs were spliced together to create a small air cavity in the center of the tapered area, as shown in Fig. 2(e). Fig. 2(f) shows the application of tensile stress. The motor was driven to a precise distance to stretch the fiber and by applying the proper discharging power for a suitable time to obtain the sensor.

Fig. 3 shows the schematic diagram and working principles of the sensor. M_1 and M_2 are the reflection surfaces of the air cavity, respectively. Light emitted from a broadband light source with intensity I_0 enters the SMF on the left to reach the glass/air reflector M_1 and is reflected the first time with intensity I_1. Some of the light propagates through the cavity and is reflected the second time by the air/glass reflecting surface M_2 with a reflected intensity of I_2. The two reflected light beams are coupled into the SMF core to yield the stable interference phenomenon manifested by strong and weak intensity distributions in the overlapping region. Because the reflectivity of glass–air is less than 4%, it can be regarded as two beam interference, namely Fabry–Pérot interference. Considering the half wave loss, the expression of the total reflected light intensity is:

$$I = I_1 + I_2 + 2\sqrt{I_1 I_2}\cos(\theta). \tag{1}$$

where θ is the phase difference of the two reflected light beams. The expression of the free spectral range (FSR) of RRAFPI interference fringes is:

$$FSR = \lambda_{m+1} - \lambda_m, \text{ and} \tag{2}$$

$$FSR = \frac{\lambda_m \lambda_{m+1}}{2nL_{FP}}. \tag{3}$$

where m is the interference series of FPI, λ_m is the FPI resonance wavelength of the corresponding interference series, n is the refractive index of air, and L_{FP} is the length of the air cavity.

The strain acts on the air cavity directly to change L_{FP} and causes a spectral drift with the following relationship:

$$\triangle\lambda = k_{FP}\varepsilon_{FP}. \tag{4}$$

where k_{FP} is the strain sensitivity of the air cavity. According to the theoretical analysis, the strain coefficient of the structure near the interference peak of 1550 nm is 1.55 pm/$\mu\varepsilon$ and ε_{FP} is the strain imposed by the air cavity shown in Eq. (5) [28]:

$$\varepsilon_{FP} = \frac{\triangle L_{FP}}{L_{FP}}. \tag{5}$$

Since the length of the air cavity is equal to the length of the optical fiber, the length change is measured by the volume change of the air cavity as follows:

$$\triangle\lambda = \varepsilon_{FP} E V_{FP} = \varepsilon_{fiber} E V_{fiber}. \tag{6}$$

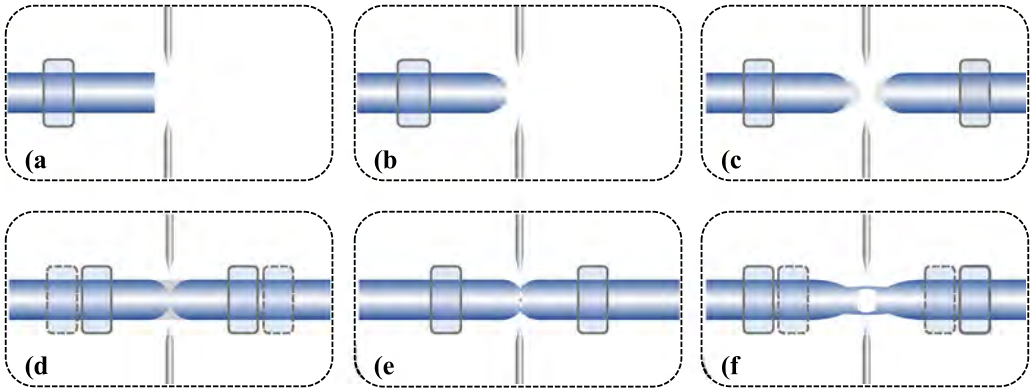

Fig. 2. Schematics showing the fabrication of the RRAFPI.

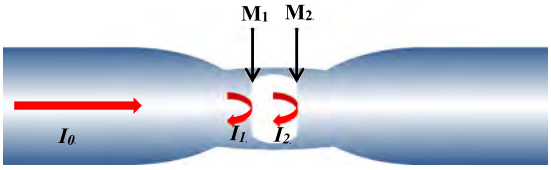

Fig. 3. Schematic diagram showing the air cavity in the RRAFPI.

where E is Young's modulus and V is the volume of the corresponding part of the subscript. The cross-sectional area is:

$$\triangle\lambda = \varepsilon_{FP} E\pi(d_{fiber}^2 - d_{FP}^2) = \varepsilon_{fiber} E\pi d_{fiber}^2. \tag{7}$$

where d is the radius of the section corresponding to the subscript. By combining these equations, the strain relationship between the sensor and air cavity can be obtained as follows:

$$\varepsilon = \frac{L_{FP} + L_{fiber}\frac{d_{fiber}^2 - d_{FP}^2}{d_{fiber}^2}}{L_{FP} + L_{fiber}}\varepsilon_{FP}. \tag{8}$$

Based on Eqs. (3) and (7), the expression of the strain sensitivity of the sensor can be obtained:

$$k = \frac{\triangle\lambda}{\varepsilon} = k_{FP}\frac{L_{FP} + L_{fiber}}{L_{FP} + L_{fiber}\frac{d_{fiber}^2 - d_{FP}^2}{d_{fiber}^2}}. \tag{9}$$

In the RRAFPI, the wall thickness is reduced to increase the air radius. Eq. (8) shows that the radius of the air cavity is directly proportional to the strain sensitivity of the sensor and the radius increases with the strain sensitivity.

The interference contrast [29] is the ratio of the difference between the maximum and minimum intensities of the interference fringes to the sum of the maximum and minimum intensity as shown by Eq. (10):

$$K = \frac{I_M - I_m}{I_M + I_m}. \tag{10}$$

where I_M and I_m are $I_1 = I_2 = I_0$, respectively. The corresponding maximum and minimum values are expressed by the following equations:

$$I_M = 2I_0(1 + \cos\theta), \text{ and} \tag{11}$$

$$I_m = 2I_0(1 - \cos\theta). \tag{12}$$

When the minimum of the interference intensity $I_m = 0$ and $K = 1$, the two light beams are fully coherent and the stripes are clearest. When $I_M = I_m$ and $K = 0$, the two beams are completely uncorrelated and show interference stripes. When $I_M \neq I_m \neq 0$ and $0 < K < 1$, the two light beams are partially coherent and the sharpness of the interference fringes is between the above two cases. Therefore, only when θ is close to 90° do the interference fringes become and the higher the interference contrast. The RRAFPI has a good reflection surface of the air cavity thereby making the angle between the incident light and reflector closer to 90° resulting significant improvement in the interference contrast.

3. Experimental measurements

In order to study the strain characteristics of RRAFPI, an optical fiber strain setup is established as shown in Fig. 4. The distance between the two three-dimensional (3D) moving platforms was set to be 10 cm. The RRAFPI was connected to the SuperK COMPACT (SC, 450–2500 nm) and optical spectrum analyzer (OSA, resolution 0.02 nm) by a 3 dB circulator to acquire the reflection spectra. The RRAFPI was placed between the 3D moving platforms and moved axially to the right in steps of 10 μm steps. Tensile stress was applied to the sensor and the strain was increased by 100 $\mu\varepsilon$.

4. Results and discussion

Fig. 5(a) presents the strain results at room temperature. When an axial strain is applied to the sensor from 0 $\mu\varepsilon$ to 1200 $\mu\varepsilon$ with a step of 200 $\mu\varepsilon$, the reflectance spectrum shows a significant red shift and the total wavelength shift reaches about 20 nm. Since the RRAFPI has a good reflection surface, Fig. 5(a) shows that the interference contrast is improved significantly to 25 dB and λ_m = 1,549.8 nm and λ_{m+1} = 1,570.4 nm at a wavelength of 1550 nm. FSR is 20.6 nm according to Eq. (2) and the air cavity length L is 59.07 μm according to Eq. (3). The actual air cavity length is 59 μm as shown by the microscopic image which shows the calculation error is only 0.07% compared with the actual value. Fig. 5(b) shows the linear fitting of the relationship between the strain and wavelength drift of the RRAFPI at different strain levels revealing R^2 of 0.99904 and excellent linearity. According to the fitted results, the wavelength drift is directly proportional to the strain applied to the sensor and the slope indicates that the strain sensitivity of the sensor is 8.0 pm/$\mu\varepsilon$.

The reproducibility of the results acquired from the RRAFPI is evaluated. The sensor undergoes a forward applied strain phase and then reverse released strain phase and the repeatability is gauged based on the stability of the strain sensitivity in the two stages. In the forward applied strain phase, the axial stress applied to the sensor increases from 0 $\mu\varepsilon$ to 1200 $\mu\varepsilon$ yielding a strain sensitivity of 8.0 pm/$\mu\varepsilon$. In the reverse releasing strain phase, the axial stress applied to the sensor is reduced from 1200 $\mu\varepsilon$ to 0 $\mu\varepsilon$, and wavelength drift is recorded every 200 $\mu\varepsilon$. By performing linear fitting for the relationship between different strain values and wavelength drift, the strain sensitivity is determined to be 7.79 pm/$\mu\varepsilon$. Fig. 6 shows that the linearly fitted

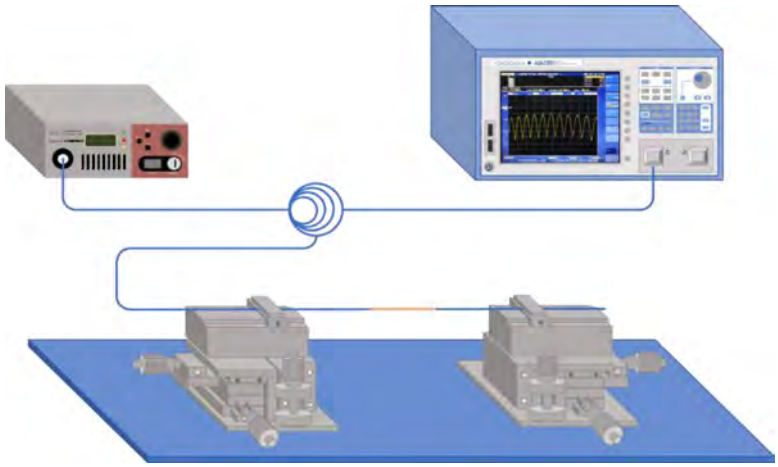

Fig. 4. Optical fiber strain l platform.

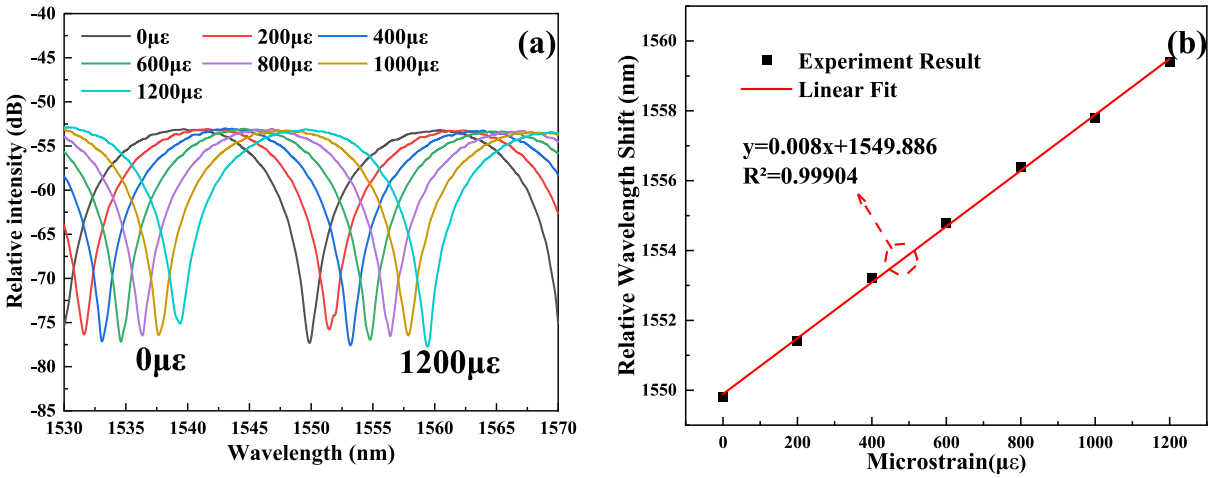

Fig. 5. Strain response of the RRAFPI: (a) Reflection spectra of the RRAFPI for different strain levels and (b) Relationship between the strain and wavelength drift of the RRAFPI.

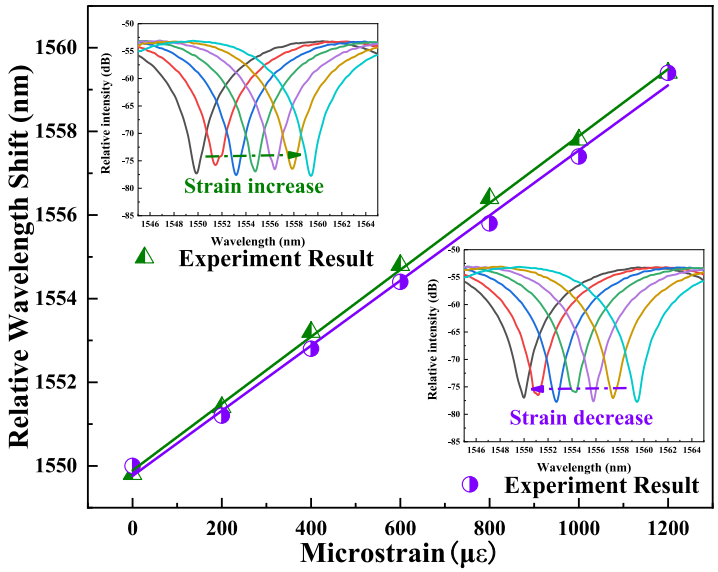

Fig. 6. Reproducibility of the results of the RRAFPI.

curves of the forward applied strain phase and reverse released strain phase basically coincide and the strain sensitivity is stable indicating good repeatability.

In order to study the temperature characteristics of RRAFPI, the sensor is immersed in a water bath to which heating is applied by an electrical heater to increase the local temperature around the sensor.

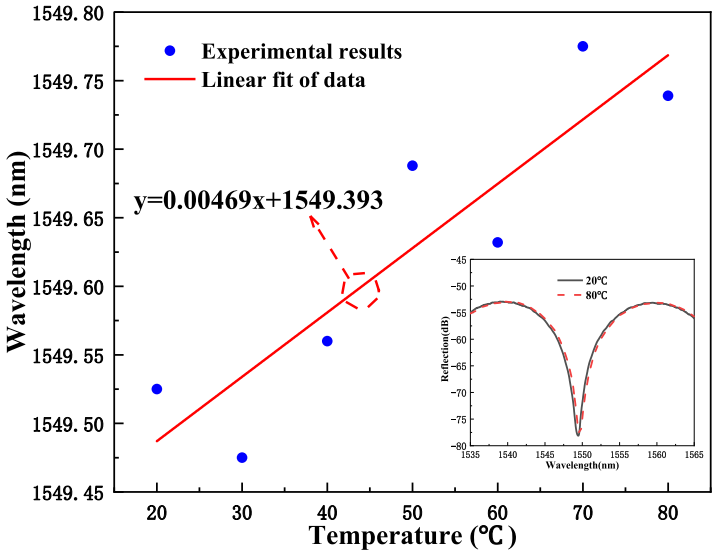

Fig. 7. Reflection results of the RRAFPI for temperature from 25 °C to 80 °C.

Table 1
Comparison of our sensor and previously reported ones.

Types	Sensitivity (pm/με)	Interference contrast (dB)	Strain range (με)	References
Strain sensor consisting of an in-fiber spherical microcavity	3.36 pm/με	4 dB	0–3000 με	[14]
Microbubble based fiber-optic FPI	4 pm/με	7 dB	0–1000 με	[15]
In-fiber FPI with an air cavity	6 pm/με	14 dB	0–1000 με	[16]
FPI with special air cavity	3.29 pm/με	20 dB	0–1100 με	[17]
Hollow microsphere FPI	4.66 pm/με	6 dB	0–1200 με	[18]
A sapphire derived fiber based FPI	1.19 pm/με	16.65 dB	0–1000 με	[19]
FPI based on an alumina ceramic derived fiber	1.5 pm/με	6 dB	0–3000 με	[20]
Unsymmetrical air-microbubble FPI	10.15 pm/με	5 dB	0–1200 με	[21]
Rounded Rectangular Air-cavity FPI	8 pm/με	25 dB	0–1200 με	This work

The sensor temperature is increased from 20 °C to 80 °C with a step size of 10 °C. As shown in Fig. 7, although the temperature is increased by 60 °C, its reflection spectrum fluctuates only in the ± 2.4 nm range. Data fitting yields the relationship between the spectral shift and temperature and the temperature sensitivity is determined to be 4.69 pm/°C as shown in Fig. 7. Based on the strain sensitivity determined previously, the strain-temperature cross-sensitivity of the sensor is derived to be about ~0.59 $\mu\varepsilon$/°C, revealing that the sensor is not very sensitive to the temperature.

To illustrate the advantages of the strain sensor, the sensitivity, interference contrast, and strain range of the sensor are compared to those of sensors reported in the recent literature, as shown in Table 1 and Fig. 8. The RRAFPI has higher interference contrast and strain sensitivity than others [14–21]. This is because RRAFPI is structurally superior due to the unique rounded rectangular structure with a small wall thickness as well as effective reflection surface. As a result, the strain sensitivity and interference contrast are improved significantly. More important, the sensor is simple to fabricate without requiring expensive and sophisticated equipment and dangerous chemical solvents boding well for mass production and commercial adoption.

5. Conclusion

A Fabry–Pérot interferometer strain sensor composed of a rounded rectangular air cavity with high sensitivity and interference contrast is designed and fabricated. The fabrication process involving a fiber fusion splicer is simple, economical, and safe. The sensor exhibits strain sensitivity of 8 pm/$\mu\varepsilon$ and interference contrast of 25 dB. The improvements stem from precisely control of the parameters to form the special structure with the unique air cavity. This structure can not only make the cavity have a small wall thickness, but also have a large measurement range without affecting the sensitivity. It can also make the reflection surface of the cavity wall flatter and smoother, and make the angle of the incident light close to 90°, thus significantly improving the interference contrast. The temperature strain sensitivity is only 0.59 $\mu\varepsilon$/°C implying that the temperature allowance is high and corresponding temperature-related error is small. In addition to the high strain sensitivity, high interference contrast, low temperature strain sensitivity, and good repeatability, the fabrication process is simple, cost effective, and safe boding well for commercial production. Therefore, the sensor has large potential in applications such as micro-strain monitoring.

Declaration of competing interest

The authors declare that they have no known competing financial interests or personal relationships that could have appeared to influence the work reported in this paper.

Data availability

The authors do not have permission to share data.

Acknowledgments

This work was jointly supported by the Local Universities Reformation and Development Personnel Training Supporting Project from Central Authorities, City University of Hong Kong Strategic Research Grant (SRG) [grant number 7005505], Guiding innovation Foundation of Northeast Petroleum University, China [grant number 2018YDL-02], Postdoctoral Scientific Research Development Fund, China [grant number LBH-Q20081], and Scientific Research Fund of Sichuan Province Science and Technology Department, China [grant number 2020YJ0137].

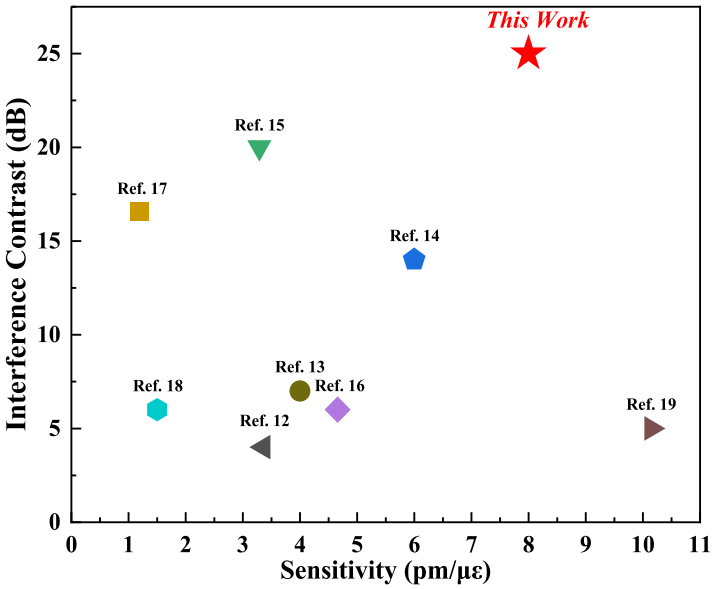

Fig. 8. Comparison of our sensor with previously reported ones.

References

[1] K. Bohnert, P. Gabus, J. Kostovic, et al., Optical fiber sensors for the electric power industry, Opt. Lasers Eng. 43 (3–5) (2005) 511–526.

[2] L. Palmieri, D. Sarchi, A. Galtarossa, Distributed measurement of high electric current by means of polarimetric optical fiber sensor, Opt. Express 23 (9) (2015) 11073–11079.

[3] W. Liu, Y. Shi, Z. Yi, et al., Surface plasmon resonance chemical sensor composed of a microstructured optical fiber for the detection of an ultra-wide refractive index range and gas-liquid pollutants, Opt. Express 29 (25) (2021) 40734–40747.

[4] W. Liu, C. Hu, L. Zhou, et al., A square-lattice D-shaped photonic crystal fiber sensor based on SPR to detect analytes with large refractive indexes, Physica E 138 (2022) 115106.

[5] G. Yilmaz, S.E. Karlik, A distributed optical fiber sensor for temperature detection in power cables, Sensors Actuators A 125 (2) (2006) 148–155.

[6] P. Roriz, S. Silva, O. Frazão, et al., Optical fiber temperature sensors and their biomedical applications, Sensors 20 (7) (2020) 2113.

[7] S. Liu, Z. Sun, L. Zhang, et al., Strain-based tunable optical microresonator with an in-fiber rectangular air bubble, Opt. Lett. 43 (17) (2018) 4077–4080.

[8] J. Tian, Z. Li, Y. Sun, et al., High-sensitivity fiber-optic strain sensor based on the vernier effect and separated Fabry-Perot interferometers, J. Lightwave Technol. 37 (21) (2019) 5609–5618.

[9] P. Ferraro, G. De Natale, On the possible use of optical fiber bragg gratings as strain sensors for geodynamical monitoring, Opt. Lasers Eng. 37 (2–3) (2002) 115–130.

[10] C.E. Campanella, A. Cuccovillo, C. Campanella, et al., Fibre bragg grating based strain sensors: review of technology and applications, Sensors 18 (9) (2018) 3115.

[11] C.L. Zhao, L. Xiao, J. Ju, et al., Strain and temperature characteristics of a long-period grating written in a photonic crystal fiber and its application as a temperature-insensitive strain sensor, J. Lightwave Technol. 26 (2) (2008) 220–227.

[12] X. Dong, H. Du, X. Sun, et al., A novel strain sensor with large measurement range based on all fiber Mach–Zehnder interferometer, Sensors 18 (5) (2018) 1549.

[13] L.M. Hu, C.C. Chan, X.Y. Dong, et al., Photonic crystal fiber strain sensor based on modified Mach–Zehnder interferometer, IEEE Photonics J. 4 (1) (2011) 114–118.

[14] E. Li, G.D. Peng, X. Ding, High spatial resolution fiber-optic Fizeau interferometric strain sensor based on an in-fiber spherical microcavity, Appl. Phys. Lett. 92 (10) (2008) 101117.

[15] D.W. Duan, Y. Rao, Y.S. Hou, et al., Microbubble based fiber-optic Fabry-Pérot interferometer formed by fusion splicing single-mode fibers for strain measurement, Appl. Opt. 51 (8) (2012) 1033–1036.

[16] S. Liu, Y. Wang, C. Liao, et al., High-sensitivity strain sensor based on in-fiber improved Fabry-Pérot interferometer, Opt. Lett. 39 (7) (2014) 2121–2124.

[17] Y. Wu, Y. Zhang, J. Wu, et al., Temperature-insensitive fiber optic Fabry-Pérot interferometer based on special air cavity for transverse load and strain measurements, Opt. Express 25 (8) (2017) 9443–9448.

[18] C. Monteiro, S. Silva, O. Frazão, Hollow microsphere Fabry-Pérot cavity for sensing applications, IEEE Photonics Technol. Lett. 29 (15) (2017) 1229–1232.

[19] P. Zhang, L. Zhang, Z. Wang, et al., Sapphire derived fiber based Fabry-Pérot interferometer with an etched micro air cavity for strain measurement at high temperatures, Opt. Express 27 (19) (2019) 27112–27123.

[20] Z. Wang, H. Liu, Z. Ma, et al., High temperature strain sensing with alumina ceramic derived fiber based Fabry-Pérot interferometer, Opt. Express 27 (20) (2019) 27691–27701.

[21] L. Cai, J. Wang, M. Chen, et al., A high-sensitivity strain sensor based on an Unsymmetrical air-microbubble Fabry-Pérot interferometer with an ultrathin wall, Measurement 181 (2021) 109651.

[22] F.C. Favero, L. Araujo, G. Bouwmans, et al., Spheroidal Fabry- Pérot microcavities in optical fibers for high-sensitivity sensing, Opt. Express 20 (7) (2012) 7112–7118.

[23] P. Ferraro, G. De Natale, On the possible use of optical fiber Bragg gratings as strain sensors for geodynamical monitoring, Opt. Lasers Eng. 37 (2–3) (2002) 115–130.

[24] C. He, C. Zhou, Q. Zhou, et al., Simultaneous measurement of strain and temperature using Fabry-Pérot interferometry and antiresonant mechanism in a hollow-core fiber, Chinese Opt. Lett. 19 (4) (2021) 041201.

[25] C. Zhou, Q. Zhou, C. He, et al., Fiber optic sensor for simultaneous measurement of refractive index and temperature based on internal-and-external-cavity Fabry-Pérot interferometer configuration, IEEE Sens. J. 21 (8) (2021) 9877–9884.

[26] H. Fu, M. Zhu, C. Liu, et al., Photonic crystal fiber supporting 394 orbital angular momentum modes with flat dispersion, low nonlinear coefficient, and high mode quality, Opt. Eng. 61 (2) (2022) 026111.

[27] H. Fu, Z. Yi, Y. Shi, et al., Circular anti-resonance fibre supporting orbital angular momentum modes with flat dispersion, high purity and low confinement loss, J. Modern Opt. 68 (15) (2021) 784–791.

[28] Y.J. Rao, M. Deng, D.W. Duan, et al., Micro Fabry-Pérot interferometers in silica fibers machined by femtosecond laser, Opt. Express 15 (21) (2007) 14123–14128.

[29] J.A. Dobrowolski, B.T. Sullivan, R.C. Bajcar, Optical interference, contrast-enhanced electroluminescent device, Appl. Opt. 31 (28) (1992) 5988–5996.